



Oxidation and wear behavior of CrAlMoN with varied Mo-content for cutting Ti6Al4V

K. Bobzin¹ · C. Kalscheuer¹ · N. Stachowski¹ · J. Dege² · W. Hintze² · C. Möller² · P. Ploog²

Received: 4 June 2023 / Accepted: 18 July 2023 / Published online: 3 August 2023
© The Author(s) 2023

Abstract

The cutting of difficult to machine materials such as titanium alloys is challenging for the machining industry. In case of the titanium alloy Ti6Al4V, the properties of the material cause high temperatures, mechanical loads as well as high frequency vibrations at the cutting edge, leading to premature tool failure. The use of uncoated carbide tools is very common for machining of Ti based alloys. However, temperature active, self-lubricating physical vapor deposition (PVD) coatings like CrAlMoN showed promising results to reduce friction and wear during turning of Ti6Al4V. In the present study, self-lubricating (Cr₃₄Al₄₁Mo₂₅)N, (Cr₂₉Al₃₆Mo₃₅)N and (Cr₂₅Al₃₁Mo₄₄)N coatings were investigated on cemented carbide tools. These were deposited by a hybrid process combining direct current Magnetron Sputtering and High Power Pulsed Magnetron Sputtering. Coating morphology, thickness, chemical composition, indentation hardness and modulus at $\vartheta = 20$ °C, $\vartheta = 200$ °C, $\vartheta = 400$ °C and $\vartheta = 600$ °C as well as the oxidation behavior were analyzed. Moreover, wear development after cutting tests using a CNC-lathe was investigated. Independent of Mo-content, all coating variants possessed a dense morphology and a smooth surface topography, as well as a coating adhesion class of HF1 to the cemented carbide substrate in Rockwell indentation tests according to DIN 4856. With an increasing amount of Mo, heat treatment temperature and time, more self-lubricating molybdenum oxides such as MoO₃ and Mo₄O₁₁ were detected by Raman spectroscopy. Therefore, the coating with the highest amount of Mo possessed the highest amount of molybdenum oxides. After cutting tests, molybdenum oxides were also found on the tool flank face by Raman spectroscopy. The level of flank wear land width decreased with increasing amount of Mo.

Keywords Physical vapor deposition · Self-lubrication · Molybdenum oxide · Wear development · Turning Ti6Al4V · Coated tools

1 Introduction

Machining is an integral part of modern production chains. There are workpiece materials that cannot be machined easily or only with increased effort. One of these materials is Ti6Al4V, which is widely used in the aerospace industry because of its lightweight construction properties and its high heat resistance [1]. Ti6Al4V possesses a combination of high strength and low density that results in significant

performance improvements. This alloy exhibits exceptional heat resistance of approximately $\vartheta = 550$ °C, low thermal conductivity of $\lambda = 5.8$ W/mK, and a Young's modulus of $E = 110$ – 140 GPa. However, due to these properties, Ti6Al4V is classified as a difficult to machine material [2]. Depending on cooling conditions and cutting parameters, the low thermal conductivity of this material causes cutting temperatures in a range of 600 °C $\leq \vartheta \leq 750$ °C at the cutting edge [3]. Additionally, Ti6Al4V shows a high tendency to adhere on the cutting tool material. Moreover, the combination of high temperature strength and low Young's modulus leads to high frequency vibrations and increased stress concentrations at the cutting edge [4]. Hence, Ti6Al4V machining leads to high tool wear and build-up edge formation, as described in [5]. This leads to a lower economic efficiency of the cutting processes. Actual, cutting velocities of 30 m/min $\leq v_c \leq 60$ m/min are commonly used for longitudinal

✉ N. Stachowski
stachowski@iot.rwth-aachen.de

¹ Surface Engineering Institute (IOT), RWTH Aachen University, Kackertstr. 15, 52072 Aachen, Germany

² Institute of Production Management and Technology (IPMT), Hamburg University of Technology (TUHH), Denickestr. 17, 21073 Hamburg, Germany

turning of Ti6Al4V. In order to increase the economic efficiency of machining Ti6Al4V, a main goal is the increase of the metal removal rate Q . This can be achieved by increasing feed rate f or cutting speed v_c . However, an increase of cutting parameters also leads to increased loads at the cutting edge, resulting in early tool failure. The types of wear that occur differ depending on the type and duration of the load [2]. Due to high cutting temperatures while cutting Ti6Al4V pronounced crater wear on the rake face can be observed [6]. Crater wear in titanium machining is particularly pronounced with uncoated carbide tools due to the high affinity between titanium and carbon. This leads to a partial dissolution of the tungsten carbide, so that the released carbon diffuses to the surface and can react there with the titanium. However, the dissolution of the tungsten carbide makes the edge zone of the tool more sensitive to abrasive wear [7, 8]. Another challenge in titanium cutting is the plastic cutting edge deformation that can occur with carbide tools in the elevated temperature range [9, 10]. A frequently used approach to increase the performance of cutting tools is the application of physical vapor deposition (PVD) protective coatings [7]. Aim of PVD coatings is to separate the substrate from the Ti6Al4V, which reduces tool wear during cutting. To further decrease thermal and mechanical loads at the cutting edge, the self-lubricating effect of the coating system could be beneficial. This can be achieved within a PVD coating by combining a nitride hard coating, such as chromium aluminum nitride (CrAlN), with the transition metal molybdenum. During oxidation, transition metals like molybdenum are able to form self-lubricating phases under tribological and thermal stress. Their working mechanism is based on the formation of easily shearable planes with oxygen vacancies. This mechanism was discovered for a series of oxide phases by Arne Magnéli [11]. In the present study, self-lubricating CrAlMoN coatings with different amounts of Mo deposited on cemented carbide cutting inserts are investigated. Depending on the Mo-content, resulting coating properties as well as the oxidation behavior are analyzed. Additionally, the wear development of the coated inserts during cutting tests after defined cutting intervals of $t_c = 5$ s, $t_c = 10$ s, $t_c = 20$ s, $t_c = 40$ s, $t_c = 80$ s, $t_c = 120$ s is investigated.

2 Experimental details

2.1 Coating deposition

The coating was deposited by a hybrid process combining direct current magnetron sputtering (dcMS) and high power pulsed magnetron sputtering (HPPMS). While dcMS processes use a continuous DC voltage to cause sputtering of the coating material, HPPMS works with short voltage pulses. Among other benefits, these can

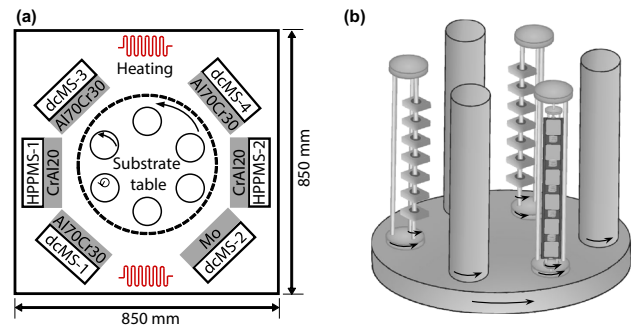


Fig. 1 Schematic representation of CemeCon CC80/9 HPPMS coating unit in top view with target configuration used (a) and the substrate table with the position of the substrate holder in threefold rotation (b)

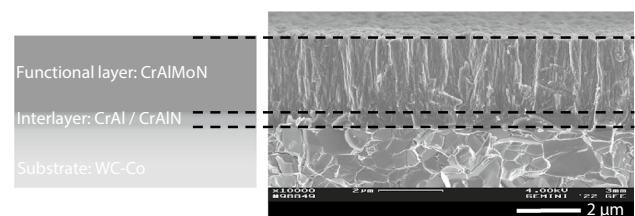


Fig. 2 Coating architecture of CrAlMoN

improve the ionization rate in processes, which improves the resulting coating properties. The deposition was carried out in a CC800/9 HPPMS CemeCon AG, Würselen, Germany, coating unit, consisting of two HPPMS and four dcMS cathodes. Targets of coating material with the dimensions $A = 500 \text{ mm} \times 88 \text{ mm}$ were installed on the cathodes. Figure 1a depicts the target configuration. The purity of the target materials was $x(\text{Al}) = 99.50\%$, $x(\text{Cr}) = 99.99\%$ and $x(\text{Mo}) = 99.99\%$. The CrAl20 target consisted of a pure chromium base plate and 20 Al plugs. Each plug had a diameter of $d = 15 \text{ mm}$. The Al70Cr30 target was produced by powder metallurgy. All coatings were deposited in a threefold substrate rotation, as shown in Fig. 1b.

The three coating variants had the same coating architecture and differed only in the Mo-content of the functional layer, Fig. 2. For better adhesion between the carbide substrate and the self-lubricating functional layer, a CrAl/CrAlN interlayer was deposited by using both HPPMS cathodes. This was followed by a smooth transition in which the process parameters of the self-lubricating functional layer were adjusted.

All six cathodes were used to deposit the functional layer. Target power was varied to achieve the variation in Mo-content. Table 1 shows the main process parameters of the functional layer for all three coating variants.

Table 1 Process parameters for coating deposition of the functional layer

Coating name	CrAlMo ₂₅ N	CrAlMo ₃₅ N	CrAlMo ₄₅ N
IOT-coating ID	ID-4398	ID-4409	ID-4397/4404
Total pressure p (mPa)	530		
Argon flow j(Ar) (sccm)	200		
Nitrogen flow j(N ₂) (sccm)	Pressure controlled		
Heating power P _H (kW)	8.0		
Bias voltage U _{Bias} (V)	– 100		
HPPMS 1—target/power P _{HPPMS-1} (kW)	CrAl20/2.5	CrAl20/2.5	CrAl20/2.5
HPPMS 2—target/power P _{HPPMS-2} (kW)	CrAl20/2.0	CrAl20/2.0	CrAl20/2.0
dcMS-1—target/power P _{dcMS-1} (kW)	Al70Cr30/2.0	Al70Cr30/2.0	Al70Cr30/2.0
dcMS-2—target/power P _{dcMS-2} (kW)	Mo/2.0	Mo/3.2	Mo/4.5
dcMS-3—target/power P _{dcMS-3} (kW)	Al70Cr30/2.5	Al70Cr30/2.5	Al70Cr30/2.5
dcMS-4—target/power P _{dcMS-4} (kW)	Al70Cr30/2.5	Al70Cr30/2.5	Al70Cr30/2.5
Deposition time t _D (s)	8575	7575	6575

2.2 Coating characterization methods

For an initial characterization, the coatings were deposited on cemented carbide inserts SNUN120408 of grade HW-K10, Kennametal Deutschland GmbH, Rossbach, Germany. Electron probe microanalysis (EPMA) was used to examine the chemical coating composition by a JEOL LXA-85, Jeol, Tokyo, Japan. Cross-section images obtained by scanning electron microscopy (SEM) were used to investigate the coating morphology and thickness. These investigations were carried out using a Zeiss DSM 982 Gemini SEM, Jena, Germany. The EPMA and the SEM analyses were performed at the Central Facility for Electron Microscopy (GFE) at RWTH Aachen University. The indentation hardness H_{IT} and the indentation modulus E_{IT} at $\vartheta = 23\text{ }^{\circ}\text{C}$, $\vartheta = 200\text{ }^{\circ}\text{C}$, $\vartheta = 400\text{ }^{\circ}\text{C}$ and $\vartheta = 600\text{ }^{\circ}\text{C}$ were measured by high temperature nanoindentation using an indentation force of $F = 8\text{ mN}$. The investigation of the indentation hardness H_{IT} and indentation modulus E_{IT} at $\vartheta = 23\text{ }^{\circ}\text{C}$ was carried out using 30 measuring points. Before analysis, the samples were smoothed by calogrinding. The analysis of the temperature influence on the indentation hardness H_{IT} and indentation modulus E_{IT} of the coatings was carried out by means of high temperature nanoindentation at $\vartheta = 200\text{ }^{\circ}\text{C}$, $\vartheta = 400\text{ }^{\circ}\text{C}$ and $\vartheta = 600\text{ }^{\circ}\text{C}$. In order to avoid the extensive wear of indenter tip, the H_{IT} and E_{IT} values at high temperatures were determined from a total of 10 force–displacement curves. The maximum measured indentation depth during nanoindentation at $\vartheta = 23\text{ }^{\circ}\text{C}$ was approximately $x = 4.76\%$ of the coating thickness. The Poisson's ratio was assumed to be $\nu = 0.25$. A Triboindenter TI 950 equipped with a heating stage xsol from Bruker Corporation, Billerica, Massachusetts, USA, was used for this purpose. The coating roughness values R_a and R_z were measured by confocal laser scanning microscopy (CLSM), VK-X 210, Keyence Corporation, Osaka, Japan. For this purpose, images of the coating

surfaces were acquired at three randomly selected positions with the CLSM at $50\times$ magnification. A measurement direction was not considered because the sample surface did not exhibit any direction-dependent texture, such as grinding marks. Subsequently, the line roughness was evaluated in the software VK Analyse-Module Version 3.4.0.1 according to ISO 4287. Here, the necessary measuring distance of $l_n = 1.25\text{ mm}$ was observed. Finally, the mean values were calculated from values determined at each of the three measuring positions. The adhesion between the coating and cemented carbide cutting insert was analyzed by Rockwell indentation tests according to DIN 4856. A Rockwell tester HP100, KNUTH Machine Tools GmbH, Wasbek, Germany, was used for this purpose. Afterwards, the indentation region was investigated by CLSM to evaluate the adhesive strength category.

2.3 Oxidation behavior

Annealing tests were carried out to determine the oxidation and diffusion behavior as a function of the Mo-content. All tests were conducted under ambient conditions for $t = 15\text{ min}$ and $t = 30\text{ min}$ at $\vartheta = 600\text{ }^{\circ}\text{C}$, $\vartheta = 700\text{ }^{\circ}\text{C}$ and $\vartheta = 800\text{ }^{\circ}\text{C}$ with a counterpart made of Ti6Al4V. The samples were placed in a heated oven. After reaching the time of the annealing experiment, the samples were taken out of the oven and cooled down to room temperature in ambient atmosphere. For heat treatment, an industrial oven Nabertherm ETH 08/17, Lilienthal, Germany was used. The experimental setup of the annealing tests is shown in Fig. 3.

The CrAlMoN coated samples were subject to a detailed analysis of the oxidation behavior. First, the coated samples were examined for geometrical and optical changes. For this purpose, the arithmetic mean roughness R_a and the average roughness R_z were first measured by means of the CLSM as explained in Sect. 2.2. Changes with regard to the coating

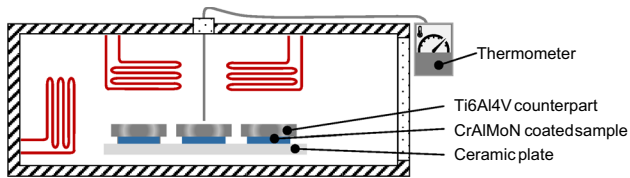


Fig. 3 Schematic representation of the experimental setup for the annealing tests

thickness, coating morphology and surface topography were studied by surface and cross-section SEM images. The SEM images were taken at the GFE at the RWTH Aachen University. The formation of oxide phases as a function of the Mo-content was analyzed by means of Raman spectroscopy. For this purpose, a Raman spectroscope, Renishaw InVia Reflex, Renishaw GmbH, Pliezhausen, Germany, with a $\lambda = 532$ nm laser and a diffraction grating g ($\lambda = 532$ nm) = 1800 l/mm was used. The measurement parameters were constant for all analyzed tools. The laser was calibrated by a reference measurement of a silicon sample before each analysis. To obtain reliable measurement results, Raman mappings with six measurements each were made on the coated surface and with three measurements on the Ti6Al4V counterparts. The focus of the Raman spectroscopy was on the detection of self-lubricating molybdenum oxides. Since the samples and tools could only be examined after cooling to room temperature, the Raman investigations with regard to the molybdenum oxides are limited to the stable phases MoO_3 , MoO_2 , and Mo_4O_{11} . Furthermore, the effects of the temperature exposure on the coating adhesion were investigated by Rockwell indentation tests.

2.4 Cutting tests

Coated cemented carbide cutting inserts CNGP 120408 of grade HW-K10, Kennametal Deutschland GmbH, Rossbach, Germany, were used to carry out the cutting tests. The cutting inserts had a corner radius of $r_e = 0.8$ mm, a cutting-edge radius of $r_p = (6 + 2) \mu\text{m}$, an effective clearance angle of $\alpha_{\text{eff}} = 6^\circ$, and an effective rake angle of $\gamma_{\text{eff}} = 2^\circ$. The cutting experiments were conducted using a CNC lathe MD5S, Gildemeister Drehmaschinen GmbH, Bielefeld, Germany. The cutting test setup as well as the tool geometry is shown in Fig. 4. The parameters of longitudinal turning of Ti6Al4V were selected in order to avoid the formation of continuous swirl chips. Therefore, a cutting velocity of $v_c = 80$ m/min, a feed rate of $f = 0.12$ mm, a cutting depth of $a_p = 1.2$ mm and a setting angle of $\kappa_r = 95^\circ$ were chosen. All tests were carried out using cooling emulsion, a mixture of distilled water and 9% cooling lubricant B-Cool 675 from Blaser Swiss-lube AG, Hasle bei Burgdorf, Switzerland. To be able to investigate the wear development, the tests were conducted

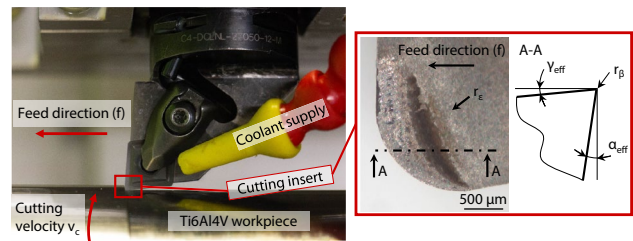


Fig. 4 Representation of the setup on the CNC lathe used for cutting tests as well as the cutting tool geometry

in defined cutting intervals of $t_c = 5$ s, $t_c = 10$ s, $t_c = 20$ s, $t_c = 40$ s, $t_c = 80$ s, $t_c = 120$ s. For each cutting interval, an unused cutting edge was tested. The tests were repeated three times.

The wear development of the rake and flank surface and the flank wear land width (VB) was measured by stereomicroscopy using a Zeiss Stemi 508, Carl Zeiss Microscopy Deutschland GmbH, Oberkochen, Germany. Additionally, the tool wear was analyzed by scanning electron microscopy (SEM) surface images. The chemical composition of the worn cutting edge areas was determined by means of energy dispersive X-ray spectroscopy (EDS) mappings. Additionally, the chips were analyzed with regard to possible diffusion processes between the CrAlMoN coatings and the workpiece material Ti6Al4V by EDS mappings. Hereby, a quantification of nitrogen, oxygen and carbon was omitted. The SEM and EDS analyses of the worn cutting edge were carried out with a Phenom XL desktop SEM, Phenom-World, Eindhoven, Netherlands. In order to examine the coating conditions after a cutting time of $t_c = 80$ s, the cutting edges cross-section was analyzed by means of focused ion beam (FIB) preparation and SEM. This FIB and SEM investigations were performed by the GFE of the RWTH Aachen University. The oxide phases formed on the coated tool surface after the cutting intervals were also investigated by Raman spectroscopy. The measurements were performed according to the same procedure as described in Sect. 2.3.

3 Results and discussion

3.1 Coating characterization

The chemical composition of the interlayer and the functional layer is shown in Fig. 5. The nitrogen content for the three variants is approximately $x_N = 50$ at.-%. This indicates an almost stoichiometric phase composition. Different studies have shown that under-stoichiometric [12] and over-stoichiometric phases [13] in PVD coatings may have a negative effect on properties such as adhesion, oxidation and diffusion behavior. The aluminum to chromium ratio of $x_{Al}/x_{Cr} \approx 1.2$

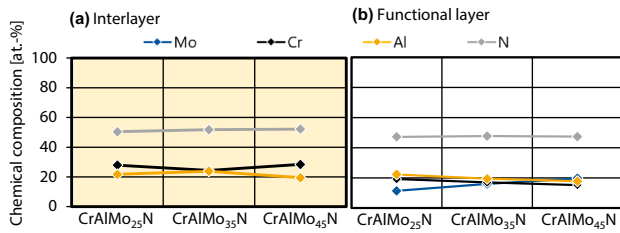


Fig. 5 Chemical composition of the interlayer (a) and the functional layer (b) for the coating variants CrAlMo₂₅N, CrAlMo₃₅N and CrAlMo₄₅N determined by EPMA analysis

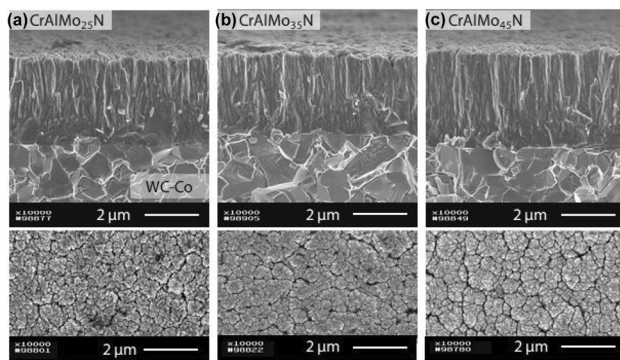


Fig. 6 SEM cross-section of CrAlMo₂₅N, CrAlMo₃₅N and CrAlMo₄₅N deposited on cemented carbide

is almost constant for all coatings. Due to the power variation of cathode dcMS-1, an increase in the amount of Mo between the coatings CrAlMo₂₅N, CrAlMo₃₅N, CrAlMo₄₅N can be seen.

The SEM cross-section images in Fig. 6 show a fine columnar morphology for all three variants. Within the cross-sections, a slight change of the very fine columnar morphology of the interlayer to a morphology with coarser columns under the graded addition of molybdenum in the functional layer is visible. However, an influence of the Mo-content of the different coatings on the columnar morphology of the functional layer could not be observed.

Table 2 lists the coating thickness as well as the surface roughness values Ra and Rz. The coating variants have an average thickness of $2.9 \mu\text{m} \leq d_s \leq 3.4 \mu\text{m}$. The measured arithmetic mean roughness values are in the range of $0.016 \mu\text{m} \leq Ra \leq 0.017 \mu\text{m}$. Also, the range of the

Table 2 Coating thickness, arithmetic mean roughness Ra and average roughness Rz of the coatings CrAlMo₂₅N, CrAlMo₃₅N and CrAlMo₄₅N

	CrAlMo ₂₅ N	CrAlMo ₃₅ N	CrAlMo ₄₅ N
Coating thickness d_s (μm)	3.3	2.9	3.4
Arithmetic mean roughness Ra (μm)	0.017 ± 0.000	0.017 ± 0.000	0.017 ± 0.000
Average roughness Rz (μm)	0.15 ± 0.01	0.17 ± 0.02	0.14 ± 0.01

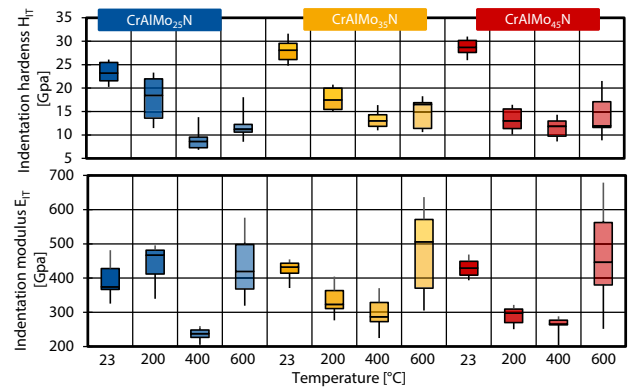


Fig. 7 Indentation hardness H_{IT} and indentation modulus E_{IT} of CrAlMo₂₅N, CrAlMo₃₅N and CrAlMo₄₅N at varied ambient temperature

determined average roughness value Rz is almost the same for CrAlMo₂₅N, CrAlMo₃₅N and CrAlMo₄₅N. Therefore, no influence of the chemical coating composition on the surface roughness is noticeable.

Figure 7 shows the indentation hardness H_{IT} and indentation modulus E_{IT} of CrAlMo₂₅N, CrAlMo₃₅N and CrAlMo₄₅N at varied ambient temperature. With increasing molybdenum content, a significant increase in indentation hardness H_{IT} from $H_{IT} = 23.2 \text{ GPa}$ to $H_{IT} = 28.3 \text{ GPa}$ and indentation modulus E_{IT} from $E_{IT} = 384 \text{ GPa}$ to $E_{IT} = 412 \text{ GPa}$ is observed. This corresponds to a percentage increase of about 22% in H_{IT} and about 12% in E_{IT} . The increase in hardness with increasing molybdenum content is possibly caused by solid solution strengthening due to lattice distortions. A comparable phenomenon was observed in [14] for CrAlMoN coating. The lattice distortions result from the substitution of the Cr and Al atoms by Mo atoms with comparatively larger atomic radius. However, it can be observed that the indentation hardness H_{IT} decreases by temperature increase from $\vartheta = 200 \text{ }^\circ\text{C}$ to $\vartheta = 400 \text{ }^\circ\text{C}$. After a further temperature increase to $\vartheta = 600 \text{ }^\circ\text{C}$, the indentation hardness H_{IT} increases slightly for all three coating variants. A comparable behavior can also be observed for the indentation modulus E_{IT} .

The bond strength between the coating and cemented carbide sample was assessed using Rockwell indentation tests following the guidelines specified in DIN 4856. Figure 8 shows the CLSM micrographs and depth profiles of these tests on the cemented carbide sample. Besides

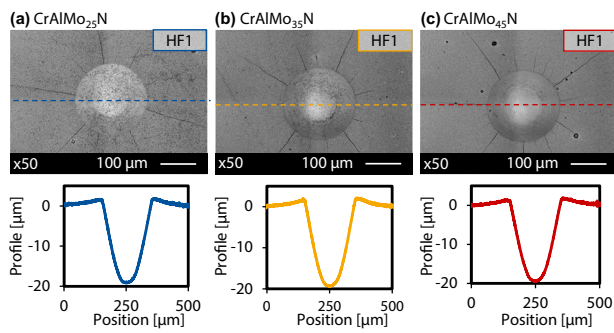


Fig. 8 CLSM micrographs and profiles of Rockwell indents of CrAlMo₂₅N, CrAlMo₃₅N and CrAlMo₄₅N on cemented carbide samples

some radial cracks around the indentation area, no coating delamination could be observed. This indicates a high adhesion strength between cemented carbide substrate and coating. Therefore, the adhesion strength of all variants is classified as adhesion class HF 1. Furthermore, the deformation of the coating-substrate compound was analyzed by means of the depth profiles of the Rockwell indentation. For all variants an almost identical deformation behavior with a maximum profile depth of $d_p = 20 \mu\text{m}$ was observed. Differences in adhesion strength or deformation due amount of Mo could not be observed.

3.2 Oxidation behavior

After annealing tests, the oxidation behavior of the three CrAlMoN coating variants were analyzed. Surface roughness values R_a and R_z were measured to determine topographical changes of the surface. Figure 9 shows a comparison of the arithmetic mean roughness R_a and the average roughness R_z of the different coating variants, annealing temperatures and times.

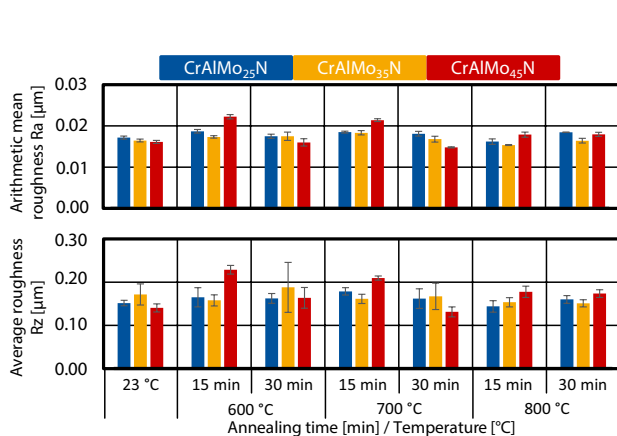


Fig. 9 Arithmetic mean roughness and average roughness of CrAlMo₂₅N, CrAlMo₃₅N and CrAlMo₄₅N after annealing

The measured values for the arithmetic mean roughness are in a range of $0.014 \mu\text{m} \leq R_a \leq 0.022 \mu\text{m}$ and the mean squared roughness R_z in a range of $0.13 \mu\text{m} \leq R_z \leq 0.23 \mu\text{m}$. The surface roughness values of the annealed samples are comparable to the initial state. No significant roughening due to strong oxide formation or due to structural changes could be identified for any of the coating variants. Figure 10 shows the SEM cross-section images of the three coating variants after heat treatment at $\vartheta_A = 700 \text{ }^\circ\text{C}$ and $\vartheta_A = 800 \text{ }^\circ\text{C}$ for $t_A = 15 \text{ min}$ and $t_A = 30 \text{ min}$. The annealing times are marked by a colored frame around the SEM images. The cross-section images of the coatings after heat treatment $\vartheta_A = 600 \text{ }^\circ\text{C}$ are not shown, because no changes in morphology were visible, compared to the as-deposited state.

After heat treatment at $\vartheta_A = 700 \text{ }^\circ\text{C}$ and $\vartheta_A = 800 \text{ }^\circ\text{C}$ for $t_A = 15 \text{ min}$ and $t_A = 30 \text{ min}$, a fine-columnar morphology can still be observed. The cross-section images of the CrAlMo₂₅N coating exhibit no visible oxidation. The surface of the CrAlMo₃₅N coated sample appears to be oxidized after annealing at $\vartheta_A = 800 \text{ }^\circ\text{C}$ for $t_A = 30 \text{ min}$. Such oxidation at the coating surface can be observed for the CrAlMo₄₅N coated samples already after annealing at $\vartheta_A = 700 \text{ }^\circ\text{C}$ for $t_A = 30 \text{ min}$. The oxidized areas were marked with dashed lines. However, the oxide layer has a thickness of only a few nanometers. Hence, there is no damage to the morphology over the entire coating thickness. The increased oxide formation with a higher Mo-content in the coating system may indicate an enhanced formation of self-lubricating molybdenum oxide phases. To analyze the oxide phase composition, the sample surfaces were examined by Raman spectroscopy after heat treatments. Since the samples can only be measured after cooling to room temperature, the Raman investigations with respect to the molybdenum oxides are limited to the phases which are stable at this temperature, such as MoO₃,

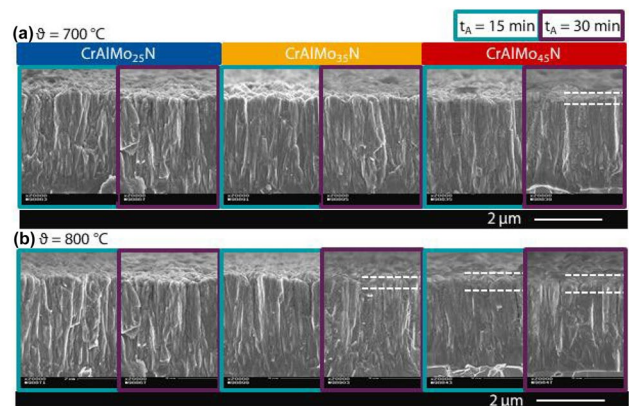


Fig. 10 SEM cross-section of CrAlMo₂₅N, CrAlMo₃₅N and CrAlMo₄₅N deposited on cemented carbide after heat treatment at $\vartheta_A = 700 \text{ }^\circ\text{C}$ and $\vartheta_A = 800 \text{ }^\circ\text{C}$ for $t_A = 15 \text{ min}$ and $t_A = 30 \text{ min}$

MoO₂, Mo₄O₁₁. Nevertheless, other metastable lubricating oxide phases may form during machining processes and contribute to an increased cutting performance. The results are presented for the coating variants CrAlMo₃₅N and CrAlMo₄₅N. No self-lubricating molybdenum oxides were detected on the surface of CrAlMo₂₅N by Raman spectroscopy. Figure 11a shows the Raman spectra of the CrAlMo₃₅N and Fig. 11b of the CrAlMo₄₅N coated samples after heat treatment at $\vartheta_A = 600\text{ }^\circ\text{C}$, $\vartheta_A = 700\text{ }^\circ\text{C}$, $\vartheta_A = 800\text{ }^\circ\text{C}$ for $t_A = 15\text{ min}$ and $t_A = 30\text{ min}$ as well as in the initial state. For better comparison, the spectra are arranged one above the other starting from the initial state. The spectra for CrAlMo₃₅N show peaks at $\dot{\nu} = 216\text{ cm}^{-1}$, $\dot{\nu} = 227\text{ cm}^{-1}$, $\dot{\nu} = 482\text{ cm}^{-1}$, $\dot{\nu} = 697\text{ cm}^{-1}$, $\dot{\nu} = 766\text{ cm}^{-1}$, which are assigned to the coating specific phases CrN [15], AlN [16], CrAlN [17], and Mo₂N [18–20] respectively. The peak at $\dot{\nu} = 331\text{ cm}^{-1}$ can be assigned to cubic Mo₂N. The intensity of the peak at $\dot{\nu} = 482\text{ cm}^{-1}$ increases with increasing temperature. This suggests that characteristic peaks at $\dot{\nu} = 461\text{ cm}^{-1}$ and $\dot{\nu} = 491\text{ cm}^{-1}$ are caused by the formation of MoO₂ [19, 20], which overlap with the peak at $\dot{\nu} = 482\text{ cm}^{-1}$. The characteristic peak of MoO₃ [20] at approximately $\dot{\nu} = 990\text{ cm}^{-1}$ can be detected for an annealing time of $t_A = 15\text{ min}$ only at $\vartheta_A = 800\text{ }^\circ\text{C}$. For an annealing time of $t_A = 30\text{ min}$, this peak is already detectable after heat treatment at $\vartheta_A = 700\text{ }^\circ\text{C}$. Principally, a peak at this position can also be attributed to the Al₂O₃. However, since it only occurs with increasing molybdenum content, presumably the oxide formation relates to molybdenum

oxides. Above the annealing temperature of $\vartheta_A = 800\text{ }^\circ\text{C}$, additional peaks at $\dot{\nu} = 929\text{ cm}^{-1}$ and at $\dot{\nu} = 932\text{ cm}^{-1}$ are detected. These peaks indicate, according to [21], the formation of AlVO₄. The AlVO₄ formed on the Ti6Al4V counterparts and adhered to the coated samples.

Similar to CrAlMo₃₅N, peaks in the spectra of CrAlMo₄₅N can be assigned to the CrN, AlN, CrAlN and Mo₂N phases. The peak at $\dot{\nu} = 479\text{ cm}^{-1}$ increases with increasing annealing temperature ϑ_A , which is due to an overlap with the peaks at $\dot{\nu} = 461\text{ cm}^{-1}$ and $\dot{\nu} = 491\text{ cm}^{-1}$. This indicates the formation of MoO₂. Regarding oxide formation, the CrAlMo₄₅N coated samples show a behavior similar to CrAlMo₃₅N. The Magnéli phase Mo₄O₁₁ with a peak position at $\dot{\nu} = 906\text{ cm}^{-1}$ is detected in all spectra. However, the intensity of the peak at $\dot{\nu} = 906\text{ cm}^{-1}$ increases with increasing annealing temperature ϑ_A and time t_A . The CrAlMo₄₅N coatings seem to form Mo₄O₁₁ at lower temperature compared to the CrAlMo₃₅N coated samples. Compared to the CrAlMo₃₅N variant, the CrAlMo₄₅N variant shows an increase in MoO₃ peak intensity corresponding to $\dot{\nu} = 988\text{ cm}^{-1}$ at lower annealing temperature and time. Furthermore, after $t_A = 15\text{ min}$, self-lubricating MoO₃ is detected from $\vartheta_A = 700\text{ }^\circ\text{C}$, indicated by the peak at $\dot{\nu} = 247\text{ cm}^{-1}$. After an annealing time of $t_A = 30\text{ min}$, further peaks at $\dot{\nu} = 290\text{ cm}^{-1}$, $\dot{\nu} = 369\text{ cm}^{-1}$ and $\dot{\nu} = 818\text{ cm}^{-1}$ are visible and assigned to molybdenum and aluminum oxides. The AlVO₄ oxide can be found after $t_A = 30\text{ min}$ from $\vartheta_A = 700\text{ }^\circ\text{C}$. Hence, increased Mo-content shifts the formation of molybdenum oxides at the coating surface towards lower annealing temperatures ϑ_A and times t_A .

The investigation of the adhesion strength after the heat treatment tests was carried out by means of the Rockwell indentation test according to DIN 4856. For all variants, after annealing at $\vartheta = 400\text{ }^\circ\text{C}$, $\vartheta = 600\text{ }^\circ\text{C}$ and $\vartheta = 800\text{ }^\circ\text{C}$ for $t = 15\text{ min}$ and $t = 30\text{ min}$, the adhesion class was HF 1. Figure 12 shows micrographs of the Rockwell indents after heat treatment at $\vartheta = 800\text{ }^\circ\text{C}$ for $t = 30\text{ min}$.

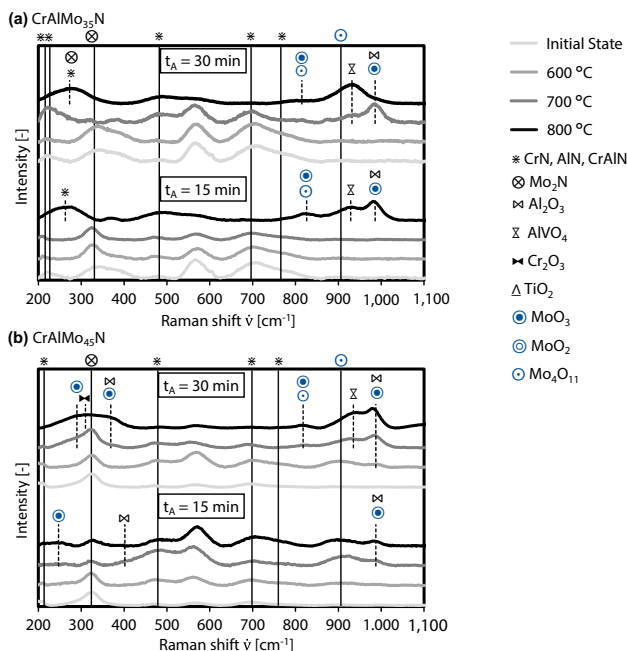


Fig. 11 Raman spectra of **a** CrAlMo₃₅N and **b** CrAlMo₄₅N deposited on cemented carbide after heat treatment

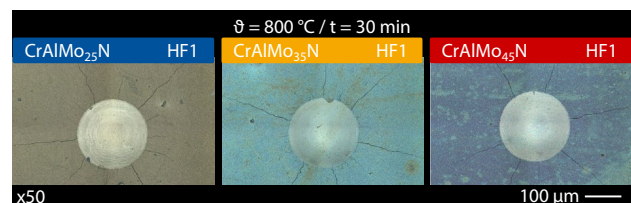


Fig. 12 CLSM micrographs of Rockwell indents of CrAlMo₂₅N, CrAlMo₃₅N and CrAlMo₄₅N on cemented carbide samples after annealing at $\vartheta = 800\text{ }^\circ\text{C}$ for $t = 30\text{ min}$

3.3 Cutting tests

For the evaluation of the wear behavior, each cutting interval was repeated three times with a new cutting edge. No significant differences in wear progress were found between the repetitions. Therefore, the representative results from one repetition are presented. To evaluate the wear behavior of the three coating variants, the flank wear land width VB was measured. The results are shown in Fig. 13 as a function of the cutting time t_c .

The wear land width increases with increasing cutting time for all coating variants. The CrAlMo₂₅N coated tools with the lowest amount of molybdenum have the highest wear land widths VB over all cutting intervals. The lowest flank wear land widths were measured for the CrAlMo₄₅N coated cutting tool. Therefore, a reduced wear at the tool flank face can be observed with increasing amount of Mo in the coating system. Whether the improved wear behavior of the coatings with the higher molybdenum content are due to the higher indentation hardness and/or a result of an improved formation of friction-reducing oxides cannot be concluded from the current state of research. Therefore, this will be the subject of further investigations.

The possibility of the formation of self-lubricating molybdenum oxides on the surface of the CrAlMo₃₅N and CrAlMo₄₅N coatings after heat treatment is discussed in Sect. 3.2. In order to clarify, whether the formation of self-lubricating molybdenum oxides is also possible in a tribological cutting contact, Raman measurements were carried out at the tool flank face near the cutting edge. A schematic representation of the measurement area as well as the results of the Raman investigations of the tools with the coating CrAlMo₄₅N are shown in Fig. 14 for selected cutting times t_c .

High surface roughness and impurities on the cutting edge, which are caused by the turning process, made it difficult to determine the phase composition. The evaluated spectra show peaks at $\tilde{\nu} = 903 \text{ cm}^{-1}$, which can be assigned to MoO₃. Furthermore, peaks are observed at $\tilde{\nu} = 322 \text{ cm}^{-1}$, $\tilde{\nu} = 392 \text{ cm}^{-1}$, $\tilde{\nu} = 903 \text{ cm}^{-1}$, $\tilde{\nu} = 679 \text{ cm}^{-1}$, $\tilde{\nu} = 697 \text{ cm}^{-1}$, and $\tilde{\nu} = 785 \text{ cm}^{-1}$. These peaks indicate the formation of

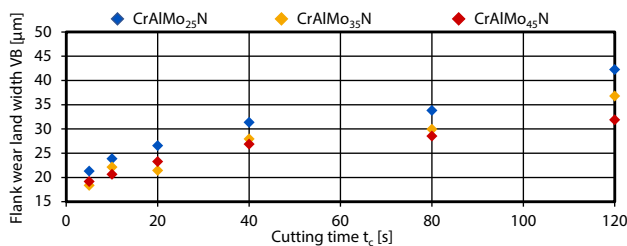


Fig. 13 Flank wear land width VB of CrAlMo₂₅N, CrAlMo₃₅N and CrAlMo₄₅N coated cutting tools as a function of the cutting time t_c

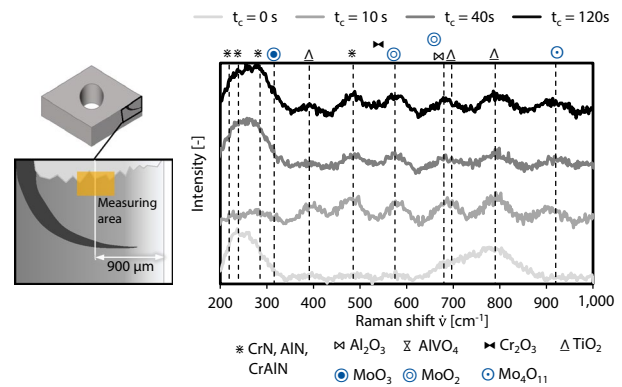


Fig. 14 Raman spectra at the tool flank surface at the yellow marked measurement area of CrAlMo₄₅N coated cutting tools after the cutting intervals

self-lubricating MoO₂ and Mo₄O₁₁ oxides, as well as the oxides Cr₂O₃, Al₂O₃ [22], AlVO₄, and TiO₂ [6]. The peaks in the range $200 \text{ cm}^{-1} \leq \tilde{\nu} \leq 300 \text{ cm}^{-1}$ and at $\tilde{\nu} = 485 \text{ cm}^{-1}$ are assigned to the coating specific phases CrN, AlN and CrAlN. Unfortunately, no assignment for Mo₂N could be made, since no reliable references were available for this nitride phase.

In the following, the dominant wear mechanisms on the rake face are analyzed. The wear mechanisms were determined in a comparable manner for all coating variants. The dominant wear mechanisms are analyzed and evaluated in Fig. 15 using the example of the CrAlMo₄₅N coated tool after $t_c = 20 \text{ s}$ by means of SEM and EDS. The typical wear mechanisms and essential features as stated in [23] and [5] are marked with numbers in the SEM image, while an EDS map is shown on the right.

On the rake face, the tool wear is composed of titanium smearing due to adhesion (1), substrate exposure due to coating delamination as a result of adhesion (2) and tribochemical reactions (3). As the areas of tribochemical reaction are located at a large distance from the cutting edge, it is assumed, that they do not impact the tool cutting

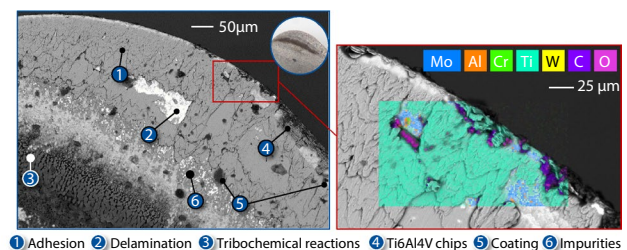


Fig. 15 SEM and EDS analyses of the tool rake face of CrAlMo₄₅N coated cutting tools after $t_c = 20 \text{ s}$

performance. Between the areas of titanium smearing and tribochemical reactions, intact coating (5) and isolated substrate exposures can be detected. Once the coating is worn out, diffusion and abrasion processes between the substrate and chip can contribute to an acceleration of crater wear. The analyses revealed that the coating is still present at the cutting edge after $t_c = 20$ s, as confirmed by EDS detection of Mo and Cr. Furthermore, Ti6Al4V chips (4) and impurities (6) at the cutting edges are distributed over the entire tool. Figure 16 shows the investigation of the rake face and cutting edge after $t_c = 80$ s for the three coating variants. For all coating variants, coating can still be detected. The substrate exposures expand towards the cutting edge with increasing cutting time.

The EDS mappings at the cutting edge, Fig. 16, support the impression of an improved wear resistance of the coatings with increasing molybdenum content. For the tools with the CrAlMo₃₅N and CrAlMo₄₅N coating, significantly more Cr and Mo can be detected in comparison to the tools coated with CrAlMo₂₅N. In order to analyze the coating condition directly at the cutting edge and below the titanium smearing at the rake and flank face, a portion of the cutting edge was removed by means of FIB (Fig. 17).

The SEM images indicate, that a homogeneous coating thickness distribution was achieved along the cutting edge during coating deposition (Fig. 17a). Furthermore, the process-related nanolaminate structure of the functional layer is visible. Figure 17a–c show the condition of the individual coating variants after $t_c = 80$ s. It seems that the functional layer is worn out at the cutting edge, Position x, but the interlayer is still undamaged. Towards the rake face, the residual coating thickness of the functional layer increases again significantly, see dashed lines. As expected, Ti6Al4V smearing (7) is seen above the functional layer. A titanium chip, which did not shear off due to the stoppage of cutting process, adhered to the cutting edge, position (8). Similar adhering of Ti6Al4V chips was observed for other coating variants and is therefore no indication for an increased tendency of adhesive wear. Independent of the molybdenum content, wear can be observed on the cutting edge of all three coating variants. However, compared to the other

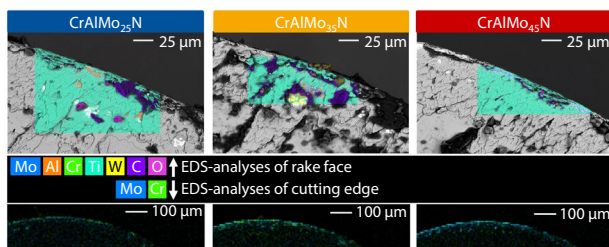


Fig. 16 EDS analyses of the tool rake face of CrAlMo₂₅N, CrAlMo₃₅N and CrAlMo₄₅N coated cutting tools after $t_c = 80$ s

variants, for the CrAlMo₂₅N coated tools, a lower residual coating thickness at the rake face can be observed, Fig. 17a. In addition, there is significantly more Ti6Al4V smearing on the rake face of the variant with CrAlMo₂₅N. Nevertheless, due to an inhomogeneous distribution of Ti6Al4V smearings along the cutting edge and small differences in position of the FIB cuts, no clear statement about the influence of the molybdenum content on the residual coating thickness is possible.

In order to detect possible diffusion between the coating and the titanium alloy Ti6Al4V, chips from the machining process were examined. Figure 18a shows a representative chip from the cutting process with a CrAlMo₄₅N coated insert after a cutting time of $t_c = 120$ s. The chip shows an irregular segmentation over the entire chip width, Fig. 18b₁. At the outside of the chip, a high degree of segmentation, which seem to be connected primarily by adhesion is visible. In contrast, the segments become narrower, Fig. 18b₂ towards the inside of the chip. Black particles adhere to the chip surface. By means of EDS those can be clearly

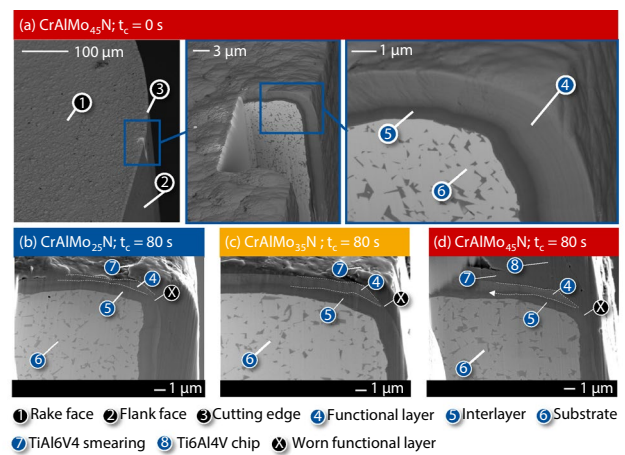


Fig. 17 Cutting edges exposed by means of FIB preparation in the initial state and after a cutting time of $t_c = 80$ s

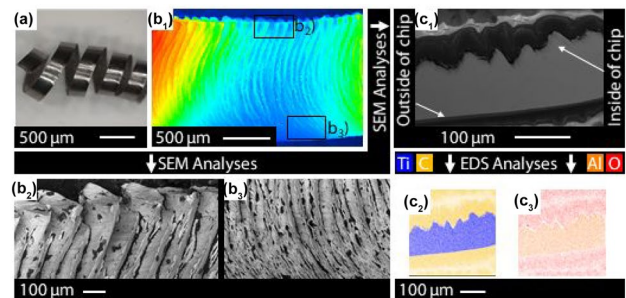


Fig. 18 Chips from a cutting process with a CrAlMo₄₅N coated insert after a cutting time of $t_c = 120$ s in total (a), as high profile (b₁) as well as after SEM and EDS analyses (b₂–c₃)

classified as contamination as a result of chip transportation. Figure 18c₁ shows a polished cross section of the chip. By EDS analysis, shown in Fig. 18c₂, c₃ only the elements titanium, carbon, aluminum and oxygen were detectable. In addition, vanadium was found. Residues of nitrogen, chromium or molybdenum were not detected during EDS mapping. Based on these findings and the fact that almost the same tribological loading is present on the underside of the chip and the resulting workpiece surface during the process, it is assumed that there is no diffusion between tool coating and Ti6Al4V during the cutting process.

4 Conclusion and outlook

In order to increase the economic efficiency and tool life while turning titanium alloy Ti6Al4V, the use of self-lubricating CrAlMoN coatings is a suitable approach. In the present study the influence of the molybdenum content on coating properties as well as the initial wear behavior while turning Ti6Al4V was analyzed. Overall, the following findings can be highlighted:

- The fine columnar morphology grows up independently of the molybdenum content. In contrast, the indentation hardness H_{IT} at $\vartheta = 23$ °C increases with increasing amount of molybdenum in the coating system.
- With increasing Mo-content and increasing annealing temperature and time an increase of self-lubricating molybdenum oxide phases on the coating surface occurs.
- The CrAlMo_{4.5}N-coated cutting tools showed the lowest flank wear. This indicates a beneficial effect on the cutting performance by increasing amount of molybdenum in the chemical composition of the coatings.
- Raman investigations showed the formation of lubricating molybdenum oxides in turning while using cooling lubricant. An increasing amount of molybdenum in the coating system promotes this trend.
- No unacceptable contamination of Ti6Al4V occurs while turning tests for the investigated coating systems.

The investigations carried out showed a distinct influence of the molybdenum content on the oxidation and wear behavior during comparatively short cutting times. Further analysis of the tool performance during turning of Ti6Al4V over an industrially standard operating period will focus on the influence of the amount of molybdenum. Following aspects will be investigated:

- Wear development of the coated cutting tools while turning Ti6Al4V over an industrially relevant application time of $20 \text{ min} \leq t_c \leq 30 \text{ min}$.

- Determination of diffusion coefficients between coating systems and Ti6Al4V by means of hot-pressing tests.
- Influence of the HPPMS fraction of the coating process on the wear resistance of the function layer of CrAlMoN coatings.

Acknowledgements The authors gratefully acknowledge the financial support of the German Research Foundation, Deutsche Forschungsgemeinschaft (DFG) within the research project “Untersuchung temperaturaktiver, reibungsmindernder Schichtsysteme für die Drehbearbeitung von Titanlegierungen”, BO 1979/69-2/HI 843/10-2, with the project number 422345568.

Funding Open Access funding enabled and organized by Projekt DEAL.

Data availability The data that support the findings of this study are available upon reasonable request from the authors.

Declaration

Conflict of interest The authors declare that they have no conflict of interest.

Open Access This article is licensed under a Creative Commons Attribution 4.0 International License, which permits use, sharing, adaptation, distribution and reproduction in any medium or format, as long as you give appropriate credit to the original author(s) and the source, provide a link to the Creative Commons licence, and indicate if changes were made. The images or other third party material in this article are included in the article's Creative Commons licence, unless indicated otherwise in a credit line to the material. If material is not included in the article's Creative Commons licence and your intended use is not permitted by statutory regulation or exceeds the permitted use, you will need to obtain permission directly from the copyright holder. To view a copy of this licence, visit <http://creativecommons.org/licenses/by/4.0/>.

References

1. Boyer RR, Cotton JD, Mohaghegh M, Schafrik RE (2015) Materials considerations for aerospace applications. *MRS Bull* 40:1055–1066. <https://doi.org/10.1557/mrs.2015.278>
2. Klocke F (2018) *Fertigungsverfahren 1: Zerspanung mit geometrisch bestimmter Schneide*, 9th edn. Springer, Berlin
3. Krämer A, Lung D, Klocke F (2012) High performance cutting of aircraft and turbine components. *AIP*, Cadiz, pp 425–432
4. Kramer BM, Viens D, Chin S (1993) Theoretical consideration of rare earth metal compounds as tool materials for titanium machining. *CIRP Ann* 42:111–114. [https://doi.org/10.1016/S0007-8506\(07\)62404-4](https://doi.org/10.1016/S0007-8506(07)62404-4)
5. Mishra SK, Ghosh S, Aravindan S (2020) Temporal and spatial crater wear prediction of WC/Co tools during dry turning of Ti6Al4V alloy. *Wear* 448–449:203229. <https://doi.org/10.1016/j.wear.2020.203229>
6. Tompsett GA, Bowmaker GA, Cooney RP, Metson JB, Rodgers KA, Seakins JM (1995) The Raman spectrum of brookite, TiO₂ (Pbca, Z = 8). *J Raman Spectrosc* 26:57–62. <https://doi.org/10.1002/jrs.1250260110>

7. Hartung PD, Kramer BM, von Turkovich BF (1982) Tool wear in titanium machining. *CIRP Ann* 31:75–80. [https://doi.org/10.1016/S0007-8506\(07\)63272-7](https://doi.org/10.1016/S0007-8506(07)63272-7)
8. Yume JAO, Kwon PY (2007) Tool wear mechanisms in machining. *IJMMM* 2:316. <https://doi.org/10.1504/IJMMM.2007.015469>
9. Davim JP (ed) (2014) *Machining of titanium alloys*. Springer, Berlin
10. Pramanik A, Islam MN, Basak A, Littlefair G (2013) Machining and tool wear mechanisms during machining titanium alloys. *AMR* 651:338–343. <https://doi.org/10.4028/www.scientific.net/AMR.651.338>
11. Magnéli A (1953) Structures of the ReO_3 -type with recurrent dislocations of atoms: 'homologous series' of molybdenum and tungsten oxides. *Acta Crystallogr* 6:495–500. <https://doi.org/10.1107/S0365110X53001381>
12. Bobzin K, Kalscheuer C, Grundmeier G, de los Arcos T, Schwiderek S, Carlet M (2021) Design of a TiAlON multilayer coating: oxidation stability and deformation behavior. *Surf Coat Technol* 421:127417. <https://doi.org/10.1016/j.surfcoat.2021.127417>
13. Schramm IC, Johansson Jöesaar MP, Jensen J, Mücklich F, Odén M (2016) Impact of nitrogen vacancies on the high temperature behavior of $(\text{Ti}_{1-x}\text{Al}_x)\text{Ny}$ alloys. *Acta Mater* 119:218–228. <https://doi.org/10.1016/j.actamat.2016.08.024>
14. Yoon CS, Kim KH, Kwon SH, Park IW (2009) Syntheses and properties of Cr-Al-Mo-N coatings fabricated by using a hybrid coating system. *J Korean Phys Soc* 54:1237–1241. <https://doi.org/10.3938/jkps.54.1237>
15. Barshilia HC, Selvakumar N, Deepthi B, Rajam KS (2006) A comparative study of reactive direct current magnetron sputtered CrAlN and CrN coatings. *Surf Coat Technol* 201:2193–2201. <https://doi.org/10.1016/j.surfcoat.2006.03.037>
16. Barshilia HC, Rajam KS (2004) Raman spectroscopy studies on the thermal stability of TiN, CrN, TiAlN coatings and nanolayered TiN/CrN, TiAlN/CrN multilayer coatings. *J Mater Res* 19:3196–3205. <https://doi.org/10.1557/JMR.2004.0444>
17. Kaindl R, Franz R, Soldan J, Reiter A, Polcik P, Mitterer C, Sartory B, Tessedri R, O'Sullivan M (2006) Structural investigations of aluminum-chromium-nitride hard coatings by Raman microspectroscopy. *Thin Solid Films* 515:2197–2202. <https://doi.org/10.1016/j.tsf.2006.07.144>
18. AlShibane I, Daisley A, Hargreaves JSJ, Hector AL, Laassiri S, Rico JL, Smith RI (2017) The role of composition for cobalt molybdenum carbide in ammonia synthesis. *ACS Sustain Chem Eng* 5:9214–9222. <https://doi.org/10.1021/acssuschemeng.7b02168>
19. Dieterle M, Mestl G (2002) Raman spectroscopy of molybdenum oxides. *Phys Chem Chem Phys* 4:822–826. <https://doi.org/10.1039/B107046K>
20. Dieterle M, Weinberg G, Mestl G (2002) Raman spectroscopy of molybdenum oxides. *Phys Chem Chem Phys* 4:812–821. <https://doi.org/10.1039/B107012F>
21. Tian H, Wachs IE, Briand LE (2005) Comparison of UV and visible Raman spectroscopy of bulk metal molybdate and metal vanadate catalysts. *J Phys Chem B* 109:23491–23499. <https://doi.org/10.1021/jp053879j>
22. Thomas PV, Ramakrishnan V, Vaidyan VK (1989) Oxidation studies of aluminum thin films by Raman spectroscopy. *Thin Solid Films* 170:35–40. [https://doi.org/10.1016/0040-6090\(89\)90619-6](https://doi.org/10.1016/0040-6090(89)90619-6)
23. Chowdhury M, Bose B, Yamamoto K, Shuster LS, Paiva J, Fox-Rabinovich GS, Veldhuis SC (2020) Wear performance investigation of PVD coated and uncoated carbide tools during high-speed machining of TiAl6V4 aerospace alloy. *Wear* 446–447:203168. <https://doi.org/10.1016/j.wear.2019.203168>

Publisher's Note Springer Nature remains neutral with regard to jurisdictional claims in published maps and institutional affiliations.